Journal of Alloys and Compounds 856 (2021) 157399

Contents lists available at ScienceDirect

Journal of Alloys and Compounds

journal homepage: http://www.elsevier.com/locate/jalcom

Novel reduced-activation TiVCrFe based high entropy alloys

A.W. Carruthers [a, *], B.S. Li [b], M. Rigby [a], L.C. Raquet [c], R. Mythili [d], C. Ghosh [d], A. Dasgupta [d], D.E.J. Armstrong [b], A.S. Gandy [c], E.J. Pickering [a]

[a] Department of Materials, University of Manchester, Manchester, M13 9PL, UK
[b] Department of Materials, University of Oxford, Oxford, OX2 6HT, UK
[c] Department of Materials Science and Engineering, University of Sheffield, Sheffield, S1 3JD, UK
[d] Metallurgy and Materials Group, Indira Gandhi Centre for Atomic Research, Kalpakkam, 603102, India

ARTICLE INFO

Article history:
Received 24 February 2020
Received in revised form
11 September 2020
Accepted 28 September 2020
Available online 28 September 2020

Keywords:
High entropy alloy
Intermetallic
SEM EBSD & EDX
Laves phase
Fusion

ABSTRACT

The conditions inside next-generation nuclear reactors are likely to be extreme. High-performance materials will be required, and there is still great scope for developing new and improved alloys. High-entropy alloys (HEAs) are potential candidates, and it is likely that such alloys will need to be based around low-activation elements that tend to form body-centred cubic structures. Whilst there have been a number of investigations assessing the capability of CALPHAD databases to predict the phases formed in face-centred cubic HEAs, their applicability to less studied systems is not well known. Here, two low-activation HEAs are produced; TiVCrMnFe and $Si_{0.1}TiVCr_{0.5}Fe$, and their microstructures assessed and compared to CALPHAD predictions. The microstructures of both alloys comprised a C14 Laves phase and a B2 phase following casting, and a C14 Laves phase and a BCC solid solution (A2) phase following holding at 1200 °C, with high proportions of both constituent phases found in each case. It was found experimentally that the Laves phases in both alloys were quaternary intermetallics of Fe, V, Cr and Ti, with Fe, V and Cr likely disordered across the Fe site. These observations were compared with predictions made using four CALPHAD databases. The accuracy of the predictions varied markedly between the databases. It was found that the Laves phase was underpredicted, often severely, by the databases that did not account for the quinary nature of phase. Removing Ti from TiVCrMnFe resulted in an equiatomic VCrMnFe alloy that formed a single BCC phase at 1200 °C.

1. Introduction

High entropy alloys (HEAs) are a recent class of alloys that were first brought to widespread attention in 2004 [1]. Rather than being based on one major element, HEAs are composed of 5 or more elements usually in equi- (or near equi-) atomic ratios. HEAs are so named because of their high entropies of mixing, where $\Delta S_{mix} = -R\sum c_i \ln(c_i)$ is the concentration of the c_ith element and R is the gas constant [2–5]. *i*is maximised when the proportions of elements within an alloy are equi-atomic. It is argued that a high entropy of mixing should reduce the Gibbs free energy of a single-phase solid solution and stabilise it. This should outweigh any increased propensity to form intermetallic phases, which are typically treated as compounds that are stabilised by enthalpy only [6–8]. Other parameters have been identified as being important for the formation of a single phase solid solution are the enthalpy of mixing, ΔS_{mix}, and the relative disparity in atomic radii, ΔH_{mix}[2–5]. δ

One structural application of HEAs that has received relatively little attention is for components in Generation-IV fission and fusion reactors. There are multiple design criteria for a material that will operate in extreme Gen-IV fission and fusion nuclear reactor environments. A few studies have addressed some of these criteria, such as low-neutron cross-section [9,10]. One of the most critical criteria for alloys for fusion power is that the radioactivity of the elements used decays quickly to low levels after irradiation with energetic neutrons. An indication as to the level of the activation of each element after exposure in a fusion reactor is shown in Fig. 1 [11]. The table was calculated using the FISPAT-II inventory code, assuming two full-power years of operation. The neutron spectrum used can be found in Ref. [12].

Recently, Ayyagari et al. [10] designed HEAs targeting low-activation elements, however, their alloys contained Zr, which according to Fig. 1 is predicted to decay to low-level waste (according

* Corresponding author.
E-mail address: alexander.carruthers@manchester.ac.uk (A.W. Carruthers).

https://doi.org/10.1016/j.jallcom.2020.157399

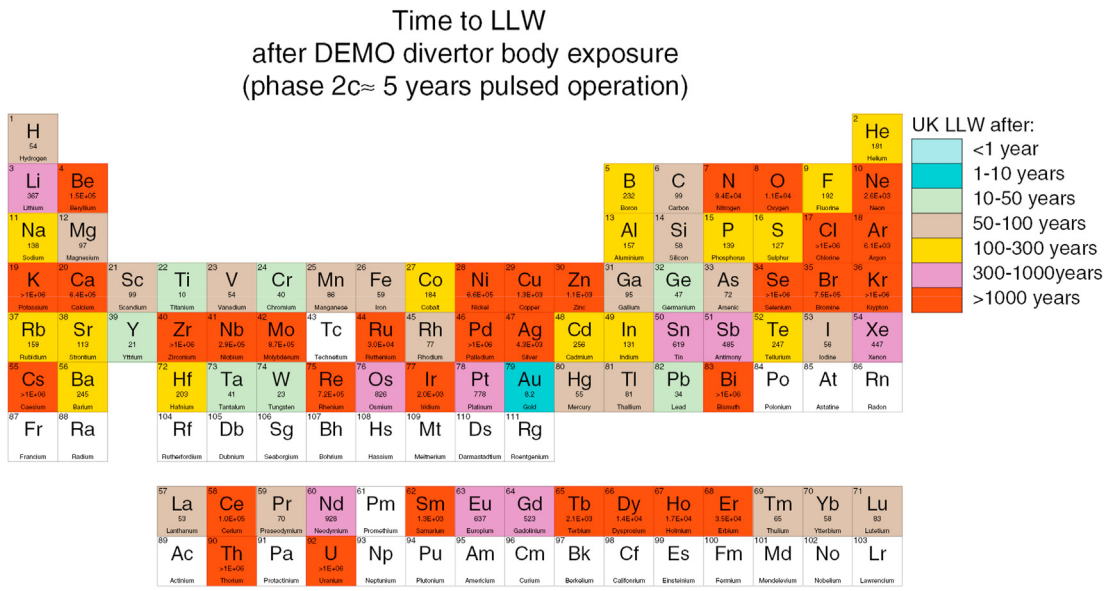

Fig. 1. Time required for each element to reach low-level activity waste (LLW) (UK low-level waste, <4 MBq kg^{-1} alpha radiation and <12 MBq kg^{-1} combined gamma and beta radiation) after ~5 years of pulsed operation in the DEMO nuclear reactor divertor body, as predicted by Gilbert et al. [11,14].

to UK standards) only after more than 1000 years in a fast-neutron fusion environment. Here, we only use elements that are predicted to decay to low levels of activity in 100 years or less in such an environment, following the work of Barron et al. [13].

Other requirements for next-generation nuclear applications include: (i) good strength and creep resistance at higher temperatures (e.g., than steels), (ii) low levels of void swelling under irradiation, and (iii) good resistance to irradiation hardening. Requirement (i) is mostly dominated by the melting point of the alloy, and hence using refractory elements is necessary. Here, we have targeted the light refractory elements V and Cr, rather than Ta and W, in order to keep density low. Resistance to void swelling, point (ii), is provided by utilising the body-centred cubic (BCC) structure over the face-centred cubic (FCC) structure. This is achieved, once again, by utilising V and Cr, which form a single bcc phase and are completely soluble with each other. The resistance to irradiation hardening, requirement (iii), is far more difficult to design for. HEAs have been proposed to have generally increased resistance to the effects of radiation due to 'sluggish diffusion' [15–20]. However, the existence of the sluggish diffusion effect in HEAs is disputed [4,21–23]. Nevertheless, it is envisaged that the chemical and microstructural complexity of HEAs may offer enhanced opportunities for defect annihilation.

A critical consideration for alloys for any structural engineering application is that their microstructures are stable and comprise the right balance of phases at the temperatures of operation (e.g., not significant fractions of embrittling intermetallic phases). In order to predict the phase stability and aid the alloy design process, CALPHAD is a powerful tool that is widely used for conventional alloys [24]. Nonetheless, its efficacy in HEA design space is less well demonstrated. A number of studies have discussed the effectiveness of databases at making predictions for FCC HEAs based on CrMnFeCoNi [25–28]. However, there have been very limited studies on other HEA systems, and no attention has been given to low-activation BCC HEAs.

In order to obtain an indication of the effectiveness of using CALPHAD to predict microstructures in low-activation BCC HEAs, in this work we compare the results of four databases to experiment for two HEA compositions. The alloy compositions studied are based on the TiVCrFe quaternary (i.e., the low-activation BCC-forming elements from the top row of the transition metals), with additions of either Mn or Si (both low-activation elements) to form quinary HEAs. Whilst it is recognised that these alloys are unlikely to have optimised compositions for engineering applications (as will become evident), their unusual compositions are useful for ascertaining the predictive power of the databases. The alloys are studied in their as-cast state and after heat treatment at 1200 °C for 100 h, with the microstructures obtained at 1200 °C being compared to the CALPHAD predictions. The resultant microstructures were characterised by scanning electron microscopy electron back-scatter diffraction (SEM-EBSD) and energy-dispersive X-ray spectroscopy (EDX), scanning transmission electron microscopy EDX (STEM-EDX) and micro-hardness. CALPHAD predictions were made in ThermoCalc using four different databases: two designed for HEAs, one designed for Fe alloys, and the other for general alloys and substances.

2. Experimental

The alloys were cast using an Arcast 200 arc melter in an Ar atmosphere. An Ar atmosphere was used preferentially to a vacuum because of the low pressure of vaporisation of Mn [29]. Elemental metals of purity >99.8% were used. The billets were flipped and remelted twice to ensure homogeneity. Table 1 shows the bulk compositions of the samples as measured in a scanning electron microscope using energy dispersive X-ray spectroscopy (SEM-EDX). Whilst equiatomic compositions were aimed for, there was significant Si and Cr loss due to evaporation in the $Si_{0.1}TiVCr_{0.5}Fe$ alloy. For each alloy, a spectrum was collected from areas, 0.2 mm^2 in size, over 1 mm apart. Both alloys were subsequently heat treated at 1200 °C for 100 h in an Ar atmosphere and quenched in water. Higher levels of Si and Cr were aimed for in the Si-containing alloy, but were lost due to evaporation during melting.

SEM characterisation of the materials was conducted using a Zeiss Sigma with Oxford Instruments EDX and EBSD detectors. Samples were mechanically polished to an OPS finish. EDX and EBSD maps were collected using a beam energy of 20 keV. All SEM-EDX maps were quantified in terms of wt.% using Oxford

Table 1
Bulk alloy contents as calculated by SEM-EDX.

at.%	Si	Ti	V	Cr	Mn	Fe
TiVCrMnFe	0	21.1 ± 0.1	19.9 ± 0.1	19.4 ± 0.1	19.7 ± 0.1	19.9 ± 0.1
$Si_{0.1}TiVCr_{0.5}Fe$	2.7 ± 0.04	24.2 ± 0.1	28.1 ± 0.6	16.4 ± 0.2	0	28.8 ± 0.9

Instruments' Aztec 4.0 software. With regards to the quantification of EDX spectra from these alloys it is noted that there is significant overlap of the kβ and kα peaks for the elements: Ti and V, V and Cr, Cr and Mn and Mn and Fe, respectively. This does not preclude quantification of the elements, but it does introduce an additional source of error that should be noted when considering results. Selected-area electron diffraction patterns (SADPs) were obtained using an FEI Talos transmission electron microscope operated at 200 keV. The error associated with lattice parameter measurements made using diffraction patterns from this instrument has been estimated to be around 5% using references with known lattice parameters. All TEM samples were prepared by twin jet electropolishing using a Tenupol with 5% perchloric acid in methanol, with the exception of the solution annealed $Si_{0.1}TiVCr_{0.5}Fe$ alloy, which was prepared via the focused Ga^+ ion beam *in-situ* lift-out method [30] using an FEI Nova Nanolab 600 SEM, operated at 30 kV and with a Ga^+ beam current of 10 pA–9 nA.

For microhardness measurements, a Matsuzawa MMT-X7A microindentor was used to make the microhardness measurements. A constant load of 1 kg was used with a 10 s dwell time, an average value of 20 measurements was reported.

CALPHAD modelling was performed using two databases within Thermocalc 2019a; the Steels/Fe-Alloys version 9.0 (TCFE9) database and the HEA database version 3.0 (HEA3). A third database, the SSOL4 database was also used with Thermocalc 2016a. All databases were used to calculate the phase proportions as a function of temperature and to predict the compositions of each phase. The compositions shown in Table 1 were used.

3. Results

3.1. As cast microstructures

In both alloys, the microstructures were found to contain two predominant phases – one forming a dendritic structure and the other filling in the interdendritic regions, see SEM-EBSD and EDX maps in Fig. 2 for TiVCrMnFe and Fig. 3 for $Si_{0.1}TiVCr_{0.5}Fe$. The interdendritic phase was identified as C14 Laves phase in both alloys, whilst the dendritic phase was found to be a B2 phase. EBSD cannot reliably distinguish between BCC and B2 structures with similar lattice parameters, but electron diffraction, Fig. 4a and Fig. 5a, confirmed the presence of a B2 structure. Although the presence of BCC areas could not be ruled out comprehensively, all areas assessed using TEM appeared chemically homogeneous and returned B2 diffraction patterns.

In both alloys, the B2 phase (dendritic regions) was found to be V and Cr rich, whilst the Laves phase (interdendritic regions) was Fe and Ti rich. The Si and Mn were both more concentrated in the Laves phase, although the Mn was to a much lesser extent. The contents of both phases as determined by SEM-EDX are given in Table 2. The B2 phases were found to have lattice parameters of 2.93 and 2.96 Å in TiVCrMnFe and $Si_{0.1}TiVCr_{0.5}Fe$ respectively.

Selected area election diffraction patterns from the interdendritic Laves phases for TiVCrMnFe and $Si_{0.1}TiVCr_{0.5}Fe$ are shown in Figs. 4b and 5b. The patterns further confirmed the presence of a C14 Laves phase, the prototype structure of which is $TiFe_2$. The lattice parameters of the Laves phases were found to be a = 4.72 Å, c = 7.72 Å and a = 4.74 Å, c = 8.13 Å in TiVCrMnFe and $Si_{0.1}TiVCr_{0.5}Fe$ respectively.

A minor third phase was also present within the microstructures of both alloys; titanium nitride, see the supplementary information, Figures S1 and S2. The nitrogen was likely a result of contamination during alloy preparation.

3.2. Microstructures after 1200 °C/100 h

SEM-EBSD and EDX maps of the microstructures of the TiVCrMnFe and $Si_{0.1}TiVCr_{0.5}Fe$ alloys after heat treating at 1200 °C for 100 h are displayed below in Fig. 6 and Fig. 7 respectively. Both alloys retained two predominant phases in their microstructures. The C14 Laves phase was again present, but the second predominant phase was found to be a BCC solid solution structure (A2), rather than a B2 phase, see SADPs in Fig. 8a and Fig. 9a. The lattice parameter of these BCC phases were found to be very similar to the B2 phases found in the as-cast state, being 2.93 and 2.94 Å in TiVCrMnFe and $Si_{0.1}TiVCr_{0.5}Fe$ respectively. SADPs of the Laves phases showed in both alloys, an increase in the a parameter and unit cell volume. The c parameter decreased in $Si_{0.1}TiVCr_{0.5}Fe$, and increased slightly in TiVCrMnFe. Lattice parameters of a = 4.84 Å, c = 7.86 Å and a = 4.98 Å, c = 8.13 Å were measured for TiVCrMnFe and $Si_{0.1}TiVCr_{0.5}Fe$ respectively.

Major differences between the as-cast and heat-treated states were seen in terms of grain size and the morphologies of the phases in the TiVCrMnFe alloy. The dendritic structure of the B2 phase seen in the as cast state has been broken up to form equiaxed grains. Figs. 2, Figs. 3, Figs. 6 and 7 have the same field of view. Multiple grains of Laves phase are visible in the matrices of the as cast states in both alloys, whereas only two and four are present in Figs. 6 and 7, respectively, after the alloys had been subjected to the high-temperature heat treatment. These observations indicate that significant diffusion has occurred at 1200 °C. No break-up of the as-cast dendritic structure was observed in $Si_{0.1}TiVCr_{0.5}Fe$, but some coarsening had evidently taken place.

The compositions of the BCC and Laves phases after 100 h at 1200 °C are shown in Table 3. A comparison with Table 2 shows that the composition of the Laves phase in both alloys remained fairly constant between the as cast and solution annealed states. Meanwhile, owing to the increase in Laves phase proportion, the BCC phase in the heat-treated state is depleted in Ti, Si and Fe and enriched in V and Cr relative to the as-cast B2 phases.

3.3. Comparison of phase proportions

The proportion of each phase (Laves and B2/BCC) as found in the EBSD maps are shown in Table 4. Note the phase fractions have been normalised to sum to 100%. A small error in the phase proportions calculated is acknowledged because the TiN are identified as the B2/BCC phase. This error is likely to be <1%, however, given that attempts to segment the Ti-rich and Fe-poor regions by thresholding in the EDX maps to find the TiN fraction yielded approximate fractions of 0.8% in both alloys. The phase proportions of Laves and BCC were consistent with those calculated from the EDX data, see supplementary information Section S2.

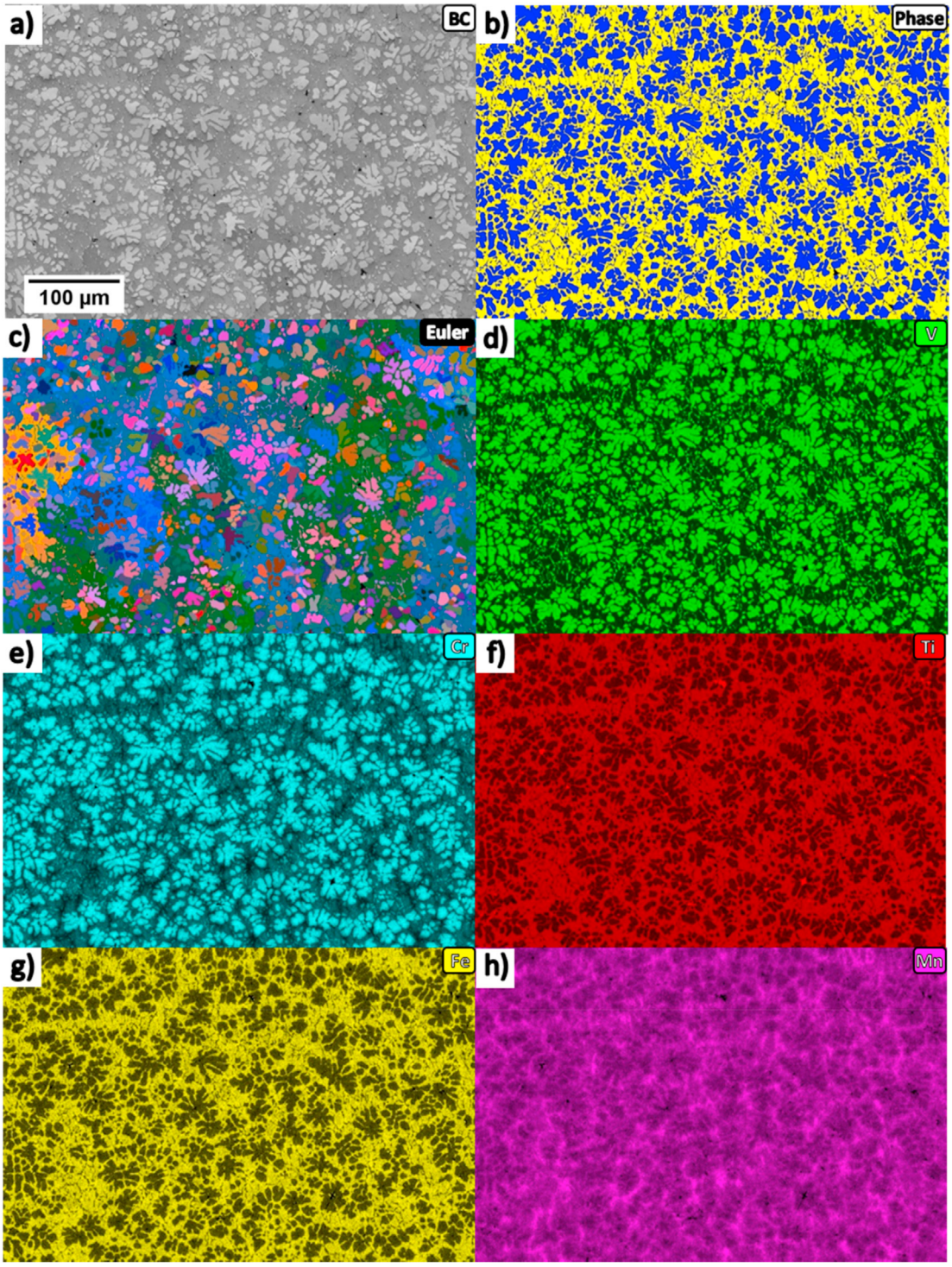

Fig. 2. a) SEM-EBSD band contrast, b) phase map (Laves = yellow, B2 = blue), c) euler angle map and d-h) EDX maps from TiVCrMnFe in the as cast state. (For interpretation of the references to colour in this figure legend, the reader is referred to the Web version of this article.)

3.4. MicroHardness

The microhardness of the alloys are recorded in Table 5. Only a small hardening change is present after heat treatment at 1200 °C. All the indents caused crack formations in the material, an example of which is shown in Fig. 10. Whilst the cracks did pass through some BCC grains, they were formed predominantly in the brittle Laves phase (even in the as-cast state), as is evidenced by the cracks deflection and bridging across the BCC phase in Fig. 10.

3.5. CALPHAD modelling

The CALPHAD predictions of the phase proportions and compositions as a function of temperature for TiVCrMnFe and $Si_{0.1}TiVCr_{0.5}Fe$ are shown in Fig. 11 and Fig. 12 respectively. Table 6 shows the compositions of the phases in TiVCrMnFe and $Si_{0.1}TiVCr_{0.5}Fe$ predicted by Thermocalc using the different databases at 1200 °C. These results can be directly compared with the experimentally observed phase compositions in Table 3. There is

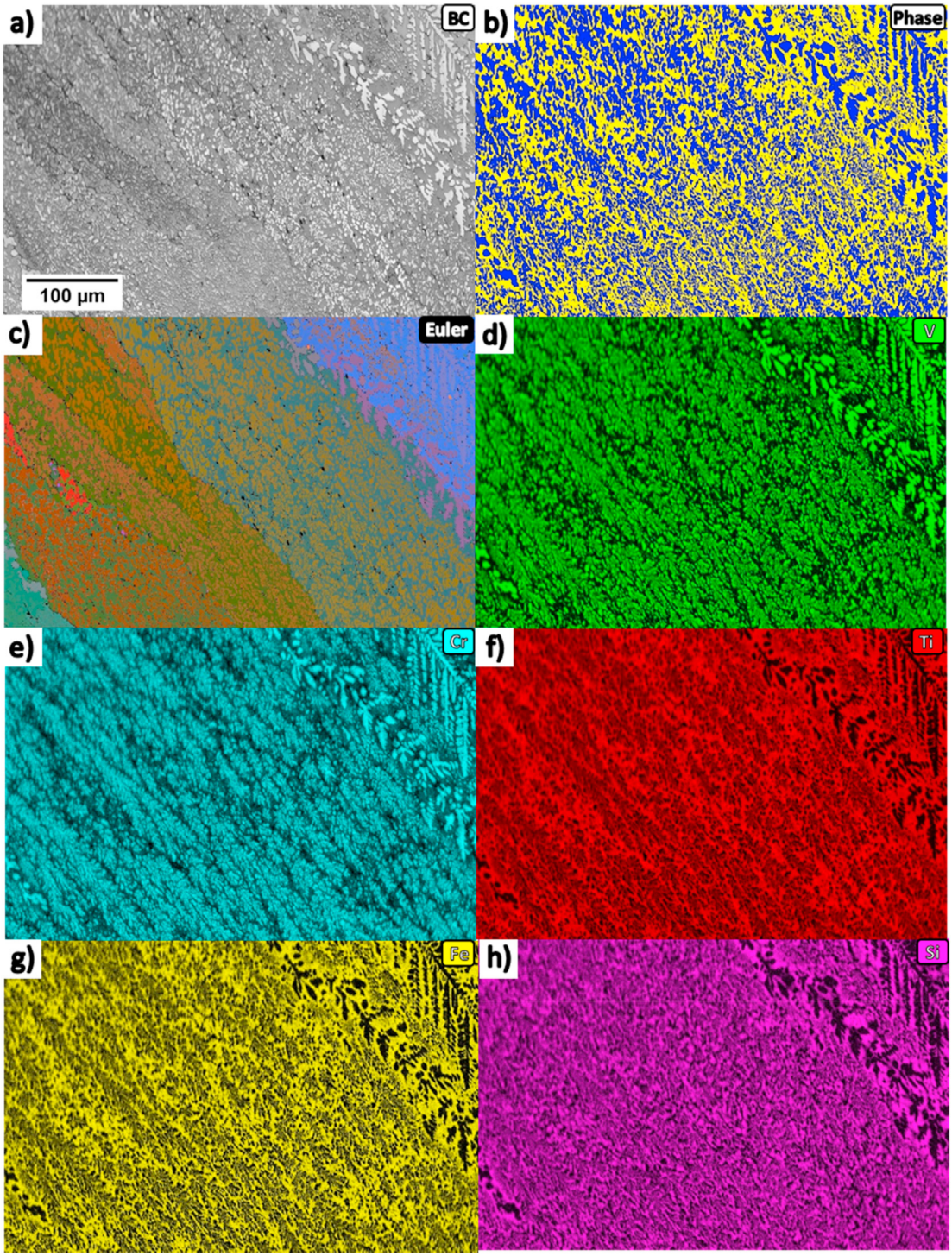

Fig. 3. a) SEM-EBSD band contrast, b) phase map (Laves = yellow, B2 = blue), c) euler angle map and d-h) EDX maps from $Si_{0.1}TiVCr_{0.5}Fe$ in the as cast state. (For interpretation of the references to colour in this figure legend, the reader is referred to the Web version of this article.)

some qualitative agreement between the predictions made by the TCFE9 and SSOL4 databases and experimental observations. For both alloys, both databases predict the formation of a BCC phase from the melt followed by the Laves phase, which is in agreement with the dendritic nature of the BCC phase in the as-cast alloys. Peaks corresponding to such events were observed in DSC traces from the two alloys - see supplementary information Section S3. With the exception of V in the Laves phase, which in turn increases the proportions of other elements predicted to be in the Laves phase, there appears to be a reasonable approximation of the proportions of each element in the BCC and Laves phases. The TCFE9 database also predicts an FeTi phase at lower temperatures, which is a B2 structure. Nevertheless, there are some significant discrepancies between the TCFE9 and SSOL4 predictions and

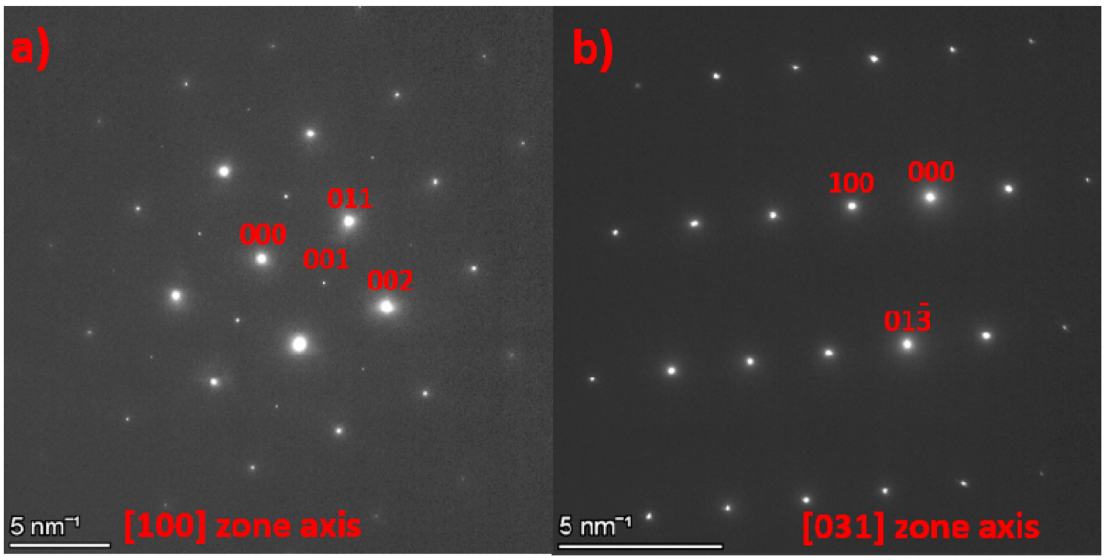

Fig. 4. SADPs from TiVCrMnFe in the as cast state of the a) B2 phase and b) Laves phase.

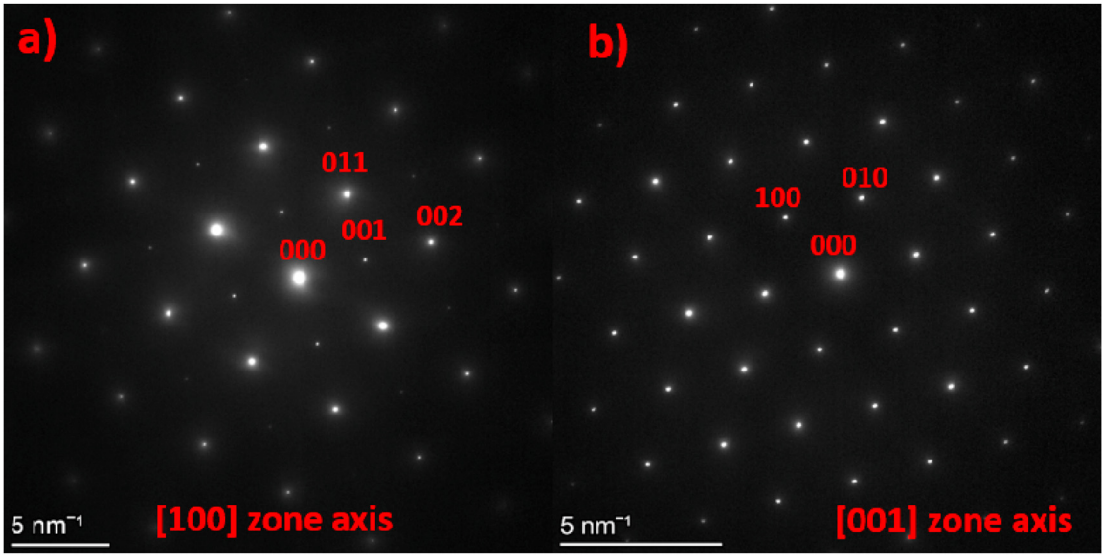

Fig. 5. SADPs from $Si_{0.1}TiVCr_{0.5}Fe$ in the as cast state of the a) B2 phase and b) Laves phase.

Table 2
Compositions of Laves and B2 phases in 'as cast' $Si_{0.1}TiVCr_{0.5}Fe$ and TiVCrMnFe. Values are given in at.%.

at.%		Si	Ti	V	Cr	Mn	Fe
TiVCrMnFe	**Laves**	0	26.7 ± 1.4	14.1 ± 1.5	16 ± 0.6	20.3 ± 0.1	22.8 ± 0.8
	B2	0	12.9 ± 0.2	28.1 ± 0.3	24.4 ± 0.2	18.8 ± 0.1	15.8 ± 0.1
$Si_{0.1}TiVCr_{0.5}Fe$	**Laves**	3.6 ± 0.1	28.4 ± 0.5	22 ± 0.9	13.9 ± 1.0	0	32.1 ± 0.8
	B2	1.4 ± 0.4	17.9 ± 1.5	37.8 ± 2.8	18.5 ± 1.1	0	24.4 ± 0.7

experiment. The fractions of Laves predicted at 1200 °C in both alloys are far below those measured. It is also clear that the solidus temperature for $Si_{0.1}TiVCr_{0.5}Fe$ may have been underestimated by TCFE9 and SSOL4, since no evidence of melting was observed in the alloy after its solution anneal.

Overall, the HEA4 database predicts the phase proportions and compositions of the alloys best, whilst the HEA3 database performs the worst. It is worth noting that the HEA4 database predicts the formation of a B2 phase at temperatures below 600 °C for both alloys. HEA3 predicts almost no Laves phase formation in either alloy at 1200 °C, instead predicting two predominant BCC phases of distinct compositions. For the TiVCrMnFe alloy, there appears to be a discontinuity between the two BCC phases around the solidus temperature. With the exception of the TCFE9 database, an unobserved M_5Si_3 phase is also predicted to form in $Si_{0.1}TiVCr_{0.5}Fe$. However, only small proportions are predicted to form at 1200 °C

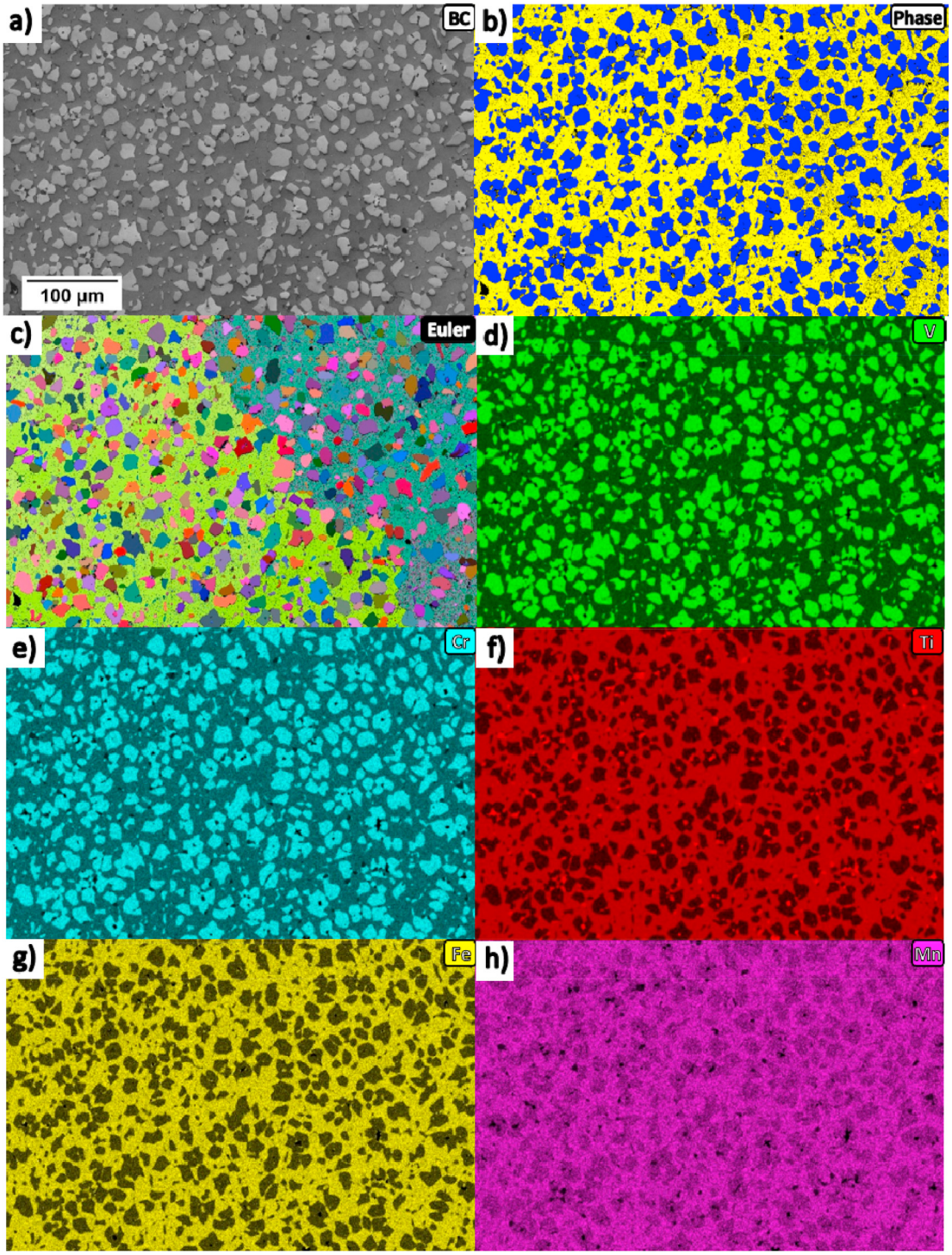

Fig. 6. a) SEM-EBSD band contrast, b) phase map (Laves = yellow, BCC = blue), c) euler angle map and d-h) EDX maps from TiVCrMnFe post solution annealing. (For interpretation of the references to colour in this figure legend, the reader is referred to the Web version of this article.)

and it is likely that the phase was not observed in as cast condition due to insufficient time for their formation during cooling.

4. Discussion

4.1. Phase stability and comparison to CALPHAD

It is quite clear that neither alloy investigated was a single-phase solid solution after casting or following heat treatment at 1200 °C. Indeed, rather than decrease the level of Laves phase, as might have been expected, the high-temperature hold at 1200 °C appeared to increase the amount of it in both alloys. This can perhaps be explained by examining the likely solidification pathway. It seems probable that the solidification progressed via a peritectic reaction, rather than eutectic growth, since no indications of coupled growth (e.g., lamellae) were observed between the primary dendrites in either alloy. In peritectic reactions, it is well known that the fraction of primary phase formed is typically in excess of the equilibrium

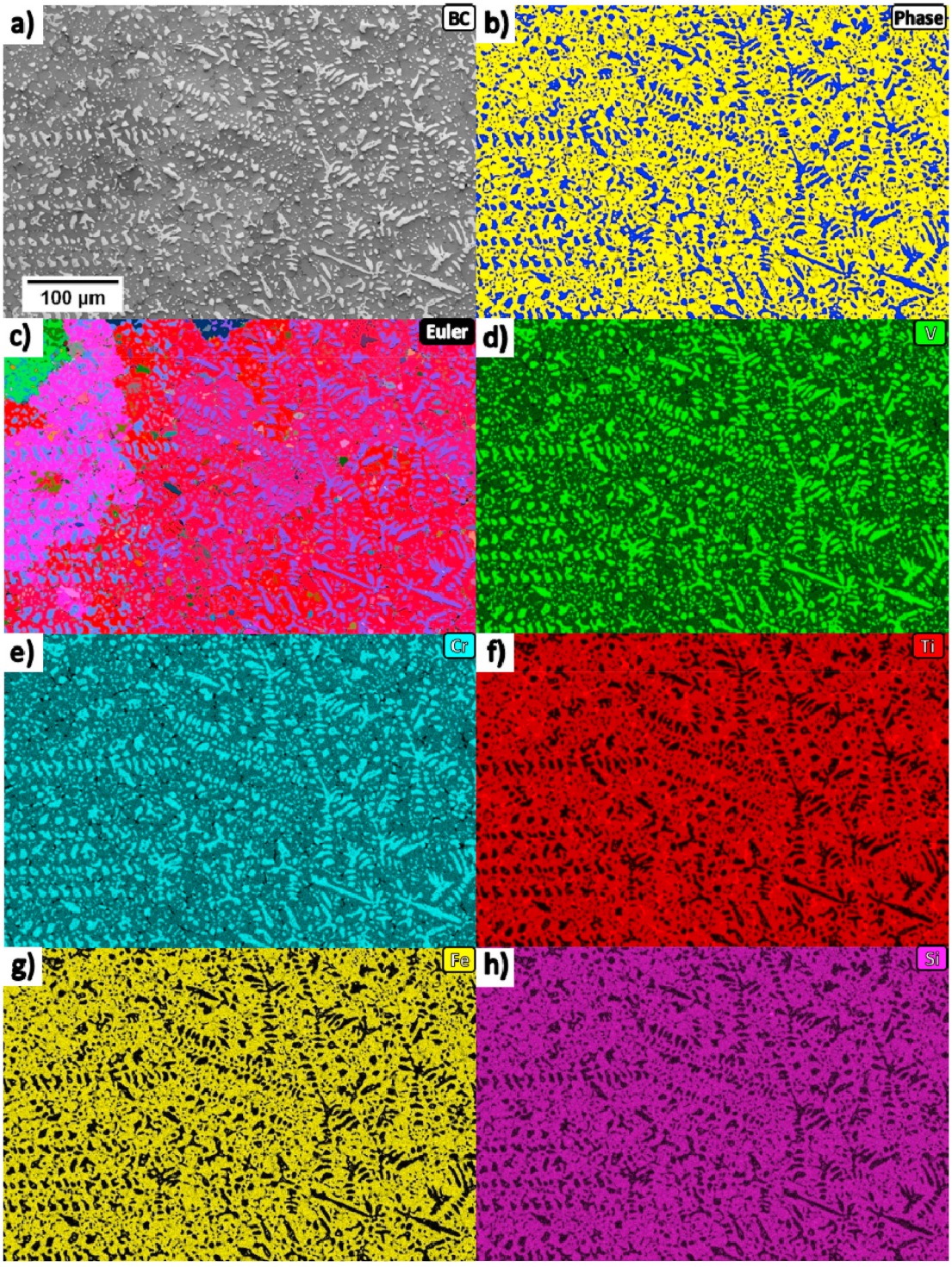

Fig. 7. a) SEM-EBSD band contrast, b) phase map (Laves = yellow, BCC = blue), c) euler angle map and d-h) EDX maps from $Si_{0.1}TiVCr_{0.5}Fe$ post solution annealing. (For interpretation of the references to colour in this figure legend, the reader is referred to the Web version of this article.)

fraction owing to inhibited transformation kinetics [31,32]. The 'over-production' of the primary phase and corresponding increase of Laves fraction on holding at high temperature (allowing for nearer-equilibrium fractions to be obtained) observed for the HEAs here are consistent with this. It is less clear why the phase fractions changed more dramatically on holding at 1200 °C for $Si_{0.1}TiVCr_{0.5}Fe$ than for TiVCrMnFe, but this may have resulted simply from the equilibrium fractions of primary dendritic phase and Laves in TiVCrMnFe being closer to those resulting from the peritectic solidification than in $Si_{0.1}TiVCr_{0.5}Fe$. It is clear from both the experimental results in Table 4 and the results of the HEA4 CALPHAD predictions in Figs. 11d and 12d that the Laves fraction is significantly higher in $Si_{0.1}TiVCr_{0.5}Fe$. It is interesting that the apparent existence of a peritectic Laves phase here is in contrast to a recent study that showed evidence of Laves formation in an HEA via eutectic growth [33], although it should be noted that a thorough

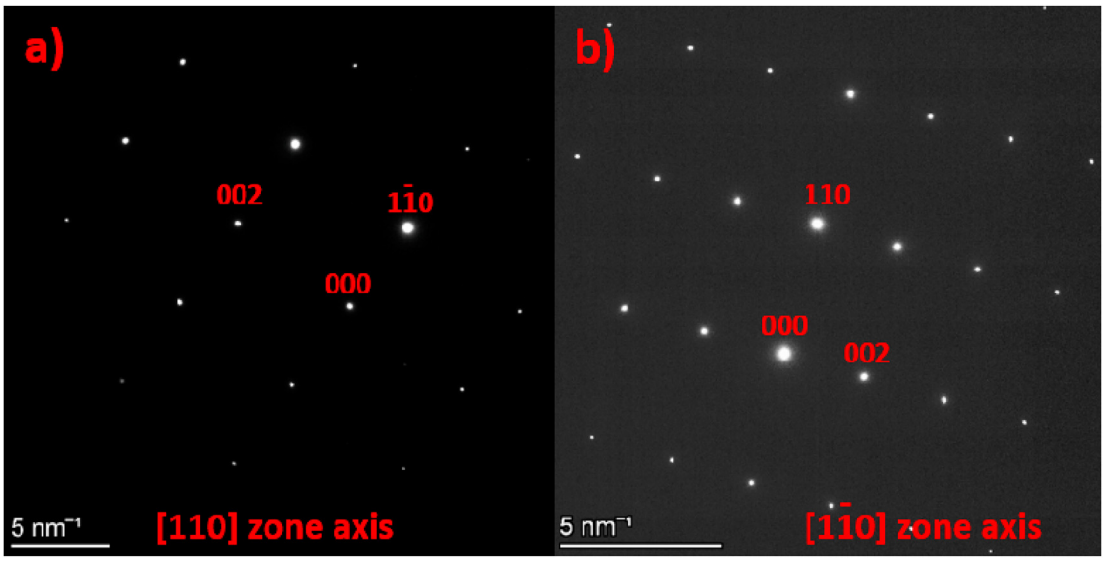

Fig. 8. SADPs from TiVCrMnFe after solution annealing of the a) BCC phase and b) Laves phase.

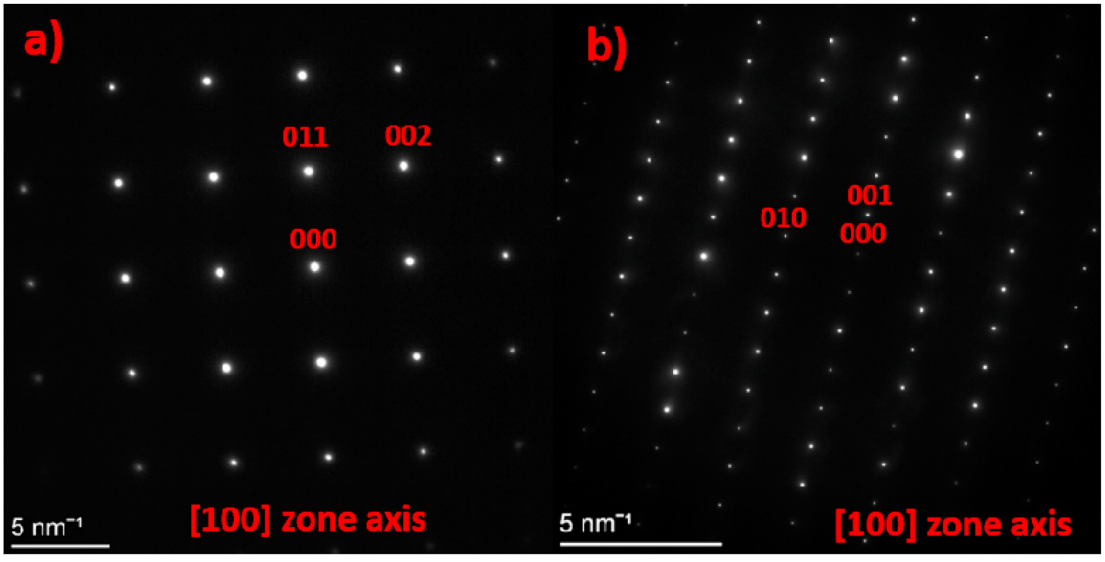

Fig. 9. SADPs from $Si_{0.1}TiVCr_{0.}$ after solution annealing of the a) BCC phase and b) Laves phase.

Table 3
Compositions of Laves and BCC phases in $Si_{0.1}TiVCr_{0.5}Fe$ and TiVCrMnFe after 100 h at 1200 °C. Values are given in at.%.

at.%		Si	Ti	V	Cr	Mn	Fe
TiVCrMnFe	**Laves**	0	28.2 ± 0.2	12 ± 0.1	15.5 ± 0.1	20.6 ± 0.1	23.8 ± 0.1
	BCC	0	8.7 ± 0.3	32.5 ± 0.3	26 ± 0.1	18.8 ± 0.1	14.1 ± 0.2
$Si_{0.1}TiVCr_{0.5}Fe$	**Laves**	3.6 ± 0.1	29.5 ± 0.4	20 ± 1.0	13.7 ± 0.3	0	33.2 ± 0.9
	BCC	0.6 ± 0.2	9.3 ± 0.8	48.3 ± 0.9	23.3 ± 0.3	0	18.5 ± 0.3

investigation was not made here to rule out the formation of Laves through a divorced eutectic at some stage of solidification.

A B2 phase was observed in the as cast state for both alloys, but not after solution annealing, where BCC solid solution predominated instead. The reasons for this were not a focus of this study and were not explored further, but the compositional changes arising during holding at 1200 °C, in combination with a fast cooling rate on water quenching from this temperature, are likely to have been responsible (the fast cooling rate preventing any

Table 4
Proportions of B2, BCC and Laves phases as found by EBSD after 100 h at 1200 °C.

	TiVCrMnFe				$Si_{0.1}TiVCr_{0.5}Fe$			
	As Cast		Post SA		As Cast		Post SA	
	Laves	B2	Laves	BCC	Laves	B2	Laves	BCC
%	51.8	48.2	57.9	42.1	53.5	46.5	70.7	29.3

Table 5
Microhardness of the alloys, with standard deviation.

	TiVCrMnFe		Si0.1TiVCr0.5Fe	
	As Cast	Post SA	As Cast	Post SA
Microhardness (HV1)	713 ± 25	685 ± 30	837 ± 33	871 ± 51

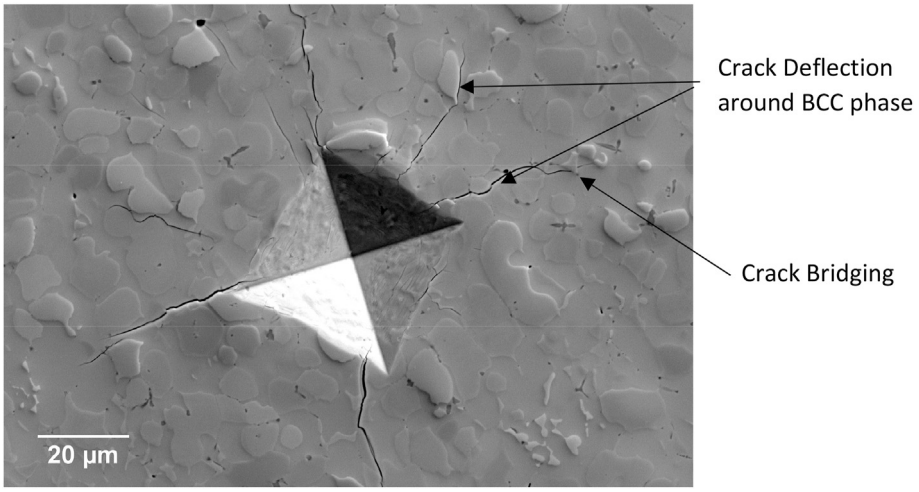

Fig. 10. Secondary electron micrograph of a micro-indent in TiVCrMnFe heat treated at 1200 °C for 100 h showing significant cracking around it.

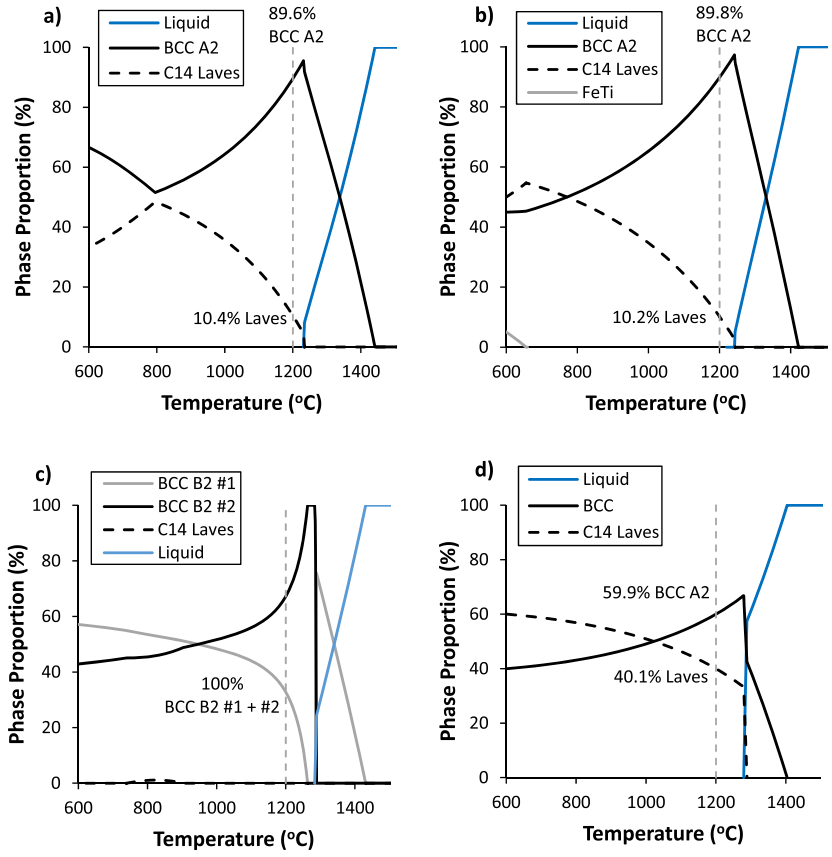

Fig. 11. Phase diagrams for TiVCrMnFe calculated using Thermocalc with a) the TCFE9 database, b) the SSOL4 database, c) the HEA3 database and d) the HEA4 database. The phase proportions predicted at 1200 °C are marked on the plots. Note, FeTi has a B2 structure.

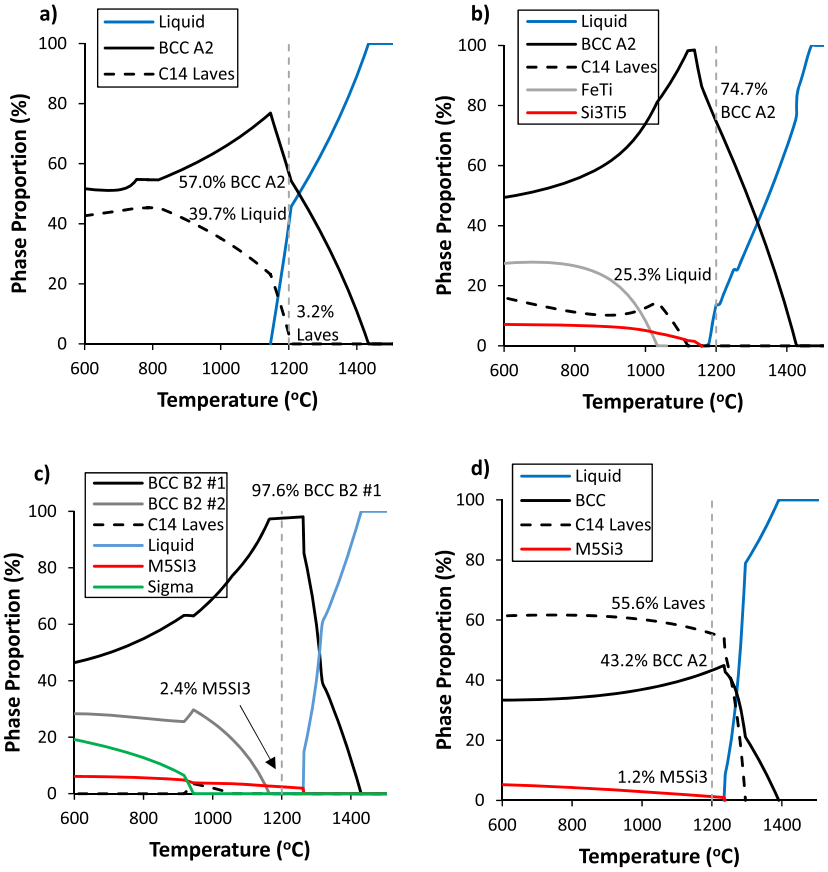

Fig. 12. Phase diagrams for $Si_{0.1}TiVCr_{0.5}Fe$ calculated using Thermocalc with a) the TCFE9 database, b) the SSOL4 database, c) the HEA3 database and d) the HEA4 database. The phase proportions predicted at 1200 °C are marked on the plots.

ordering of the BCC phase at low temperature). It seems probable that Ti is driving the ordering (the B2 predicted by some of the ThermoCalc databases at low temperatures is Ti rich), and the B2 phases in the as-cast state were found to be richer in Ti than their corresponding BCC phases in the solution-annealed state.

Table 6
Phase Compositions of BCC and Laves phases in a) TiVCrMnFe and b) $Si_{0.1}TiVCr_{0.5}Fe$ at 1200 °C as calculated by Thermocalc using the TCFE9, SSOL4, HEA3 and HEA4 databases.

a)	at.%	Ti	V	Cr	Mn	Fe
BCC	**TCFE9**	16.8	21.8	20.7	21.3	19.4
	SSLO4	19.6	22.2	20.0	19.8	18.4
	HEA3 BCC (1)	14.5	23.1	23.4	23.0	15.9
	HEA3 BCC (2)	22.7	18.5	18.3	18.5	22.0
	HEA4	11.3	28.3	25.6	22.8	12.1
Laves	**TCFE9**	30.7	0.0	12.9	18.7	37.7
	SSLO4	34.7	0.0	14.1	18.3	32.9
	HEA3	-	-	-	-	-
	HEA4	34.5	8.5	11.0	15.5	30.5

b)	at.%	Si	Ti	V	Cr	Fe
BCC	**TCFE9**	0.5	17.7	33.8	18.9	29.0
	SSLO4	1.7	19.7	32.5	19.0	27.0
	HEA3	1.7	22.4	30.3	17.3	28.3
	HEA4	1.0	9.5	46.9	27.8	14.8
Laves	**TCFE9**	1.90	30.9	0.0	10.7	56.6
	HEA4	3.1	34.1	14.6	8.4	39.8
Liquid	**TCFE9**	2.9	37.3	15.6	7.3	36.9
	SSLO4	5.5	37.4	15.2	7.9	34.0
M_5Si_3	**HEA3**	37.5	62.5	0	0	0
	HEA4	37.5	62.3	14.6	0.2	0.0

With regards to the alloys hardness; the small reduction in hardness after annealing in the TVCrMnFe alloy can be attributed to the loss of the B2 phase. That the $Si_{0.1}TiVCr_{0.5}Fe$ alloy got harder after annealing demonstrates that the increase in the Laves phase is dominant over the disordering of the B2 phase in regards to the change in hardness.

The observed presence of Laves in TiVCrMnFe is in contrast to the results of Song et al. [34] who found a mixture a BCC and an FCC phase in the same alloy. The reason for this discrepancy isn't clear, since Song et al. [34] characterised the alloy after sintering at 1150 °C, which should have delivered phase fractions close to those observed here.

The observation that the two HEAs produced here were not stable as single phase solid solutions further adds to the growing evidence that entropic stabilisation of solid solutions is not typically a dominant factor in determining the microstructures of HEAs, and that the driving forces associated with intermetallic formation are more influential.

4.2. Phase compositions

It is evident from Tables 2 and 3 that all the respective alloying elements are present in significant quantities within the Laves phases found in the alloys. From the proportion of elements in the C14 Laves phase (in Table 2), the Ti is close to its stoichiometric

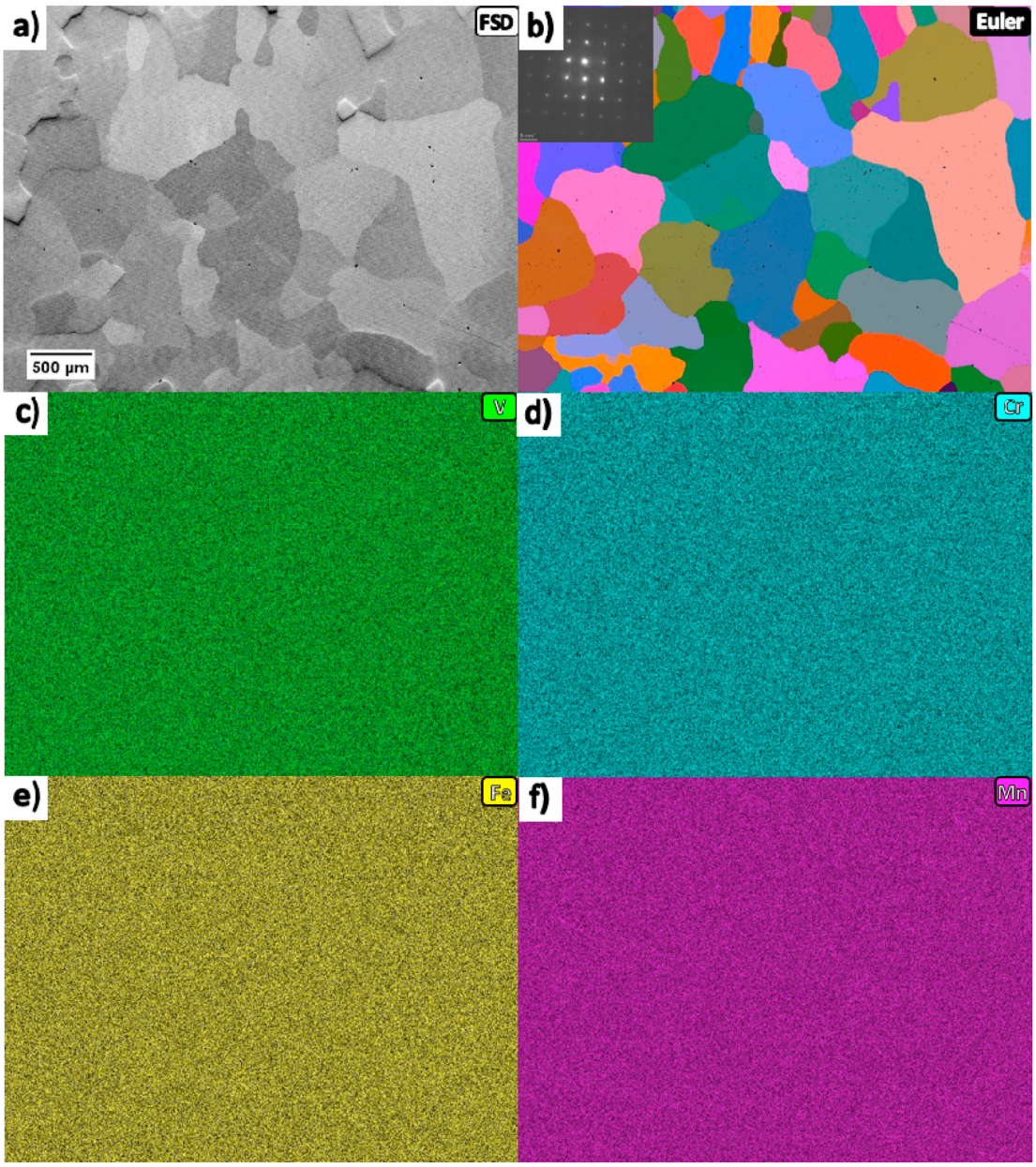

Fig. 13. a) SEM-EBSD forescatter diode (FSD) image, b) euler angle map with SADP down the [100] zone axis in the corner showing BCC A2 structure and c-f) EDX elemental maps from VCrMnFe post solution annealing. Large, equiaxed, compositionally homogenious grains of a single BCC A2 phase can be seen. All indexed points in the euler map were indexed as BCC.

concentration of 33.3 at.%. This suggests that the V, Cr, Mn and Si are predominantly substituting into Fe, rather than Ti lattice sites. The HEA4 database also corroborates this, predicting >99% occupancy of the Ti sites with Ti. Comparing the measured lattice parameters to pure Fe_2Ti [35], a and c are greater. This is consistent with the volume of the unit cell being increased due to the relatively oversized V, Cr and Mn atoms occupying Fe sites. The average atomic radii needed to make a BCC phase with a lattice constant of 3.0 Å matches the weighted average of the atomic radii of the elements that it is composed of.

Only the HEA4 database predicts significant quantities of V in the C14 Laves phases in both alloys, in agreement with the EDX results. This may explain why it performs best at predicting the phase fractions found experimentally in the alloys. Without detailed interrogation of the CALPHAD results and database behaviours, it is not possible to confirm why the inclusion of V is critical to predicting the correct Laves fraction. However, Cr, Mn and Fe all have Laves phase predicted in their binary phase diagrams with Ti, but V doesn't [36]. Thus, it may be suggested that the principal effect of the addition of V into the Laves phase serves to increase entropic stabilisation of the phase, rather than reduce enthalpy. Note that the presence of V in the Laves phase should not only increases the configurational entropy of the Laves phase, but also that of the BCC phases, by bringing its composition closer to being equi-atomic.

It has long been argued that the compositional complexity of HEAs should help to stabilise solid solutions such that intermetallics are eliminated, or at least less prevalent. However, the possibility that the compositional complexity of HEAs might act to stabilise intermetallics, entropically, as highlighted by Miracle and Senkov [21] has received relatively little attention.

4.3. Eliminating laves phase

Although the hardnesses measured for the alloys are below those for solid Laves phase [37–39], almost certainly due to the presence of the BCC phases [39], the brittle nature of the alloys will preclude them from any load-bearing structural application. The drastic reduction or removal of Laves phase is required to attain more favourable ductility.

Ti appears to be the element most responsible for stabilising the Laves phase (more so than Fe); it shows the least substitution of other elements onto its lattice sites and it shows the greatest proportionate enrichment in the Laves phase, relative to the BCC phases. An examination of the binary phase diagrams corresponding to the element combinations of Ti, V, Cr, Mn and Fe revealed that C14 Laves phase is only predicted to form in the Ti–Fe, Ti–Mn and Ti–Cr systems [36].

In order to demonstrate the influence of Ti on Laves phase stability, and to move towards an intermetallic-free composition, a third alloy was fabricated; VCrMnFe. This alloy was created and heat treatment under the same conditions as those of the other alloys investigated here. SEM-EBSD and EDX elemental maps, as well as an TEM SADP, of this material after 100 h at 1200 °C are shown in Fig. 13. Only a single BCC A2 phase was detected, with no solute segregation. Solute segregation was observed in the 'as cast' state of this alloy with Mn and Fe enriching together and V and Cr enriching together. No other phases were observed in the as cast state (including B2), however, see Figure S5 in the supplementary information. In the absence of a Laves phase, the microhardness (measured in the same way as the other alloys) was significantly lower; 354 ± 11 Hv. No cracks were observed around the indents, in contrast to the alloys reported above. These results demonstrate clearly that the removal of Ti has a profound effect on the structure, and that a single-phase BCC A2 structure is attainable with high concentrations of at least four low-activation elements.

Of course, given the abundance of σ-phase forming elements in VCrMnFe, it seems unlikely that it will remain single phase below 1200 °C. The phase diagram prediction using the HEA4 database shown in Fig. 14 certainly suggests it will decompose on ageing at intermediate temperatures. This is the subject of ongoing work.

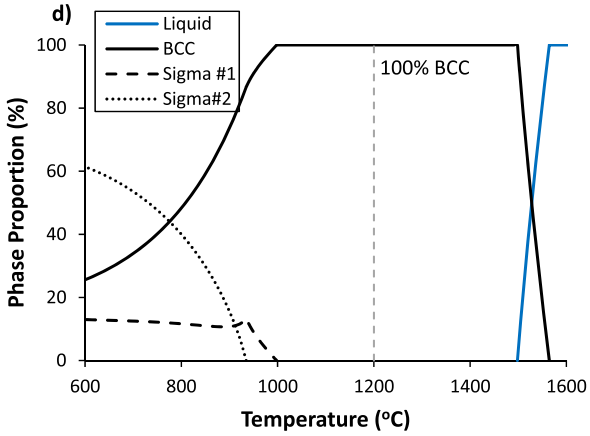

Fig. 14. Phase diagram for VCrMnFe calculated using Thermocalc with the HEA4 database. The phase proportions predicted at 1200 °C are marked on the plots.

5. Conclusions

- TiVCrMnFe and $Si_{0.5}TiVCr_{0.5}Fe$ do not form microstructures comprising a single solid solution phase in the as-cast state or after holding for 100 h at 1200 °C.
- The microstructures of both alloys were dominated by two phases in both the as-cast (B2 and C14 Laves) and after heat treatment at 1200 °C for 100 h (BCC and C14 Laves) states, with the amount of Laves increasing after holding at 1200 °C in comparison to the as-cast state.
- It is likely that Ti, and to a lesser extent Fe, were likely to responsible for stabilising the Laves C14 phase matrix within the alloys.
- The Laves phases contained significant proportions of all the elements present within the alloys. The abundance of the phase was in general poorly predicted by CALPHAD databases, apart from the HEA4 database, which was the only database to predict its quinary nature.
- Removing the Ti from the TiVCrMnFe system yielded a purely BCC A2 alloy (in the as cast state and after solution annealing at 1200 °C). This demonstrates that it is possible to obtain a single-phase BCC solid solution with at least four low-activation elements in equal concentration, although it is likely to suffer from σ phase formation at intermediate temperatures.

CRediT authorship contribution statement

A.W. Carruthers: Writing - original draft, Methodology, Investigation, Formal analysis. **B.S. Li:** Writing - review & editing, Methodology. **M. Rigby:** Methodology, Writing - review & editing. **L.C. Raquet:** Methodology, Investigation. **R. Mythili:** Software, Writing - review & editing. **C. Ghosh:** Software, Writing - review & editing. **A. Dasgupta:** Software, Writing - review & editing. **D.E.J. Armstrong:** Conceptualization, Project administration, Supervision, Writing - review & editing. **A.S. Gandy:** Conceptualization, Funding acquisition, Project administration, Supervision, Writing - review & editing. **E.J. Pickering:** Conceptualization, Project administration, Supervision, Writing - review & editing.

Declaration of competing interest

The authors declare that they have no known competing financial interests or personal relationships that could have appeared to influence the work reported in this paper.

Acknowledgements

This work was funded through EPSRC grants EP/R021864/1, EP/R021775/1 and EP/R021546/1. We also wish to acknowledge the support of the Henry Royce Institute for Advanced Materials for access to the FEI Talos electron microscope at Royce@Manchester, funded through EPSRC grants EP/R00661X/1, EP/S019367/1, EP/P025021/1 and EP/P025498/1. The raw data associated with this work can be accessed via the following link: https://zenodo.org/record/3541654#.Xc17Clf7SUk.

Appendix A. Supplementary data

Supplementary data to this article can be found online at https://doi.org/10.1016/j.jallcom.2020.157399.

References

[1] J.W. Yeh, et al., Nanostructured high-entropy alloys with multiple principal elements: novel alloy design concepts and outcomes, Adv. Eng. Mater. 6 (5) (2004) 299–303+274.
[2] X. Yang, Y. Zhang, Prediction of high-entropy stabilized solid-solution in multi-component alloys, Mater. Chem. Phys. 132 (2–3) (2012) 233–238.
[3] Y. Zhang, Y.J. Zhou, J.P. Lin, G.L. Chen, P.K. Liaw, Solid-solution phase formation rules for multi-component alloys, Adv. Eng. Mater. 10 (6) (2008) 534–538.
[4] E.J. Pickering, N.G. Jones, High-entropy alloys: a critical assessment of their founding principles and future prospects, Int. Mater. Rev. 61 (3) (2016) 183–202.
[5] W. Zhang, P.K. Liaw, Y. Zhang, A novel low-activation VCrFeTaxWx (x = 0.1, 0.2, 0.3, 0.4, and 1) high-entropy alloys with excellent heat-softening resistance, Entropy 20 (12) (2018).
[6] D.J.M. King, S.C. Middleburgh, A.G. McGregor, M.B. Cortie, Predicting the formation and stability of single phase high-entropy alloys, Acta Mater. 104 (2016) 172–179.
[7] O.N. Senkov, D.B. Miracle, A new thermodynamic parameter to predict formation of solid solution or intermetallic phases in high entropy alloys, J. Alloys Compd. 658 (2016) 603–607.
[8] M.C. Troparevsky, J.R. Morris, P.R.C. Kent, A.R. Lupini, G.M. Stocks, Criteria for predicting the formation of single-phase high-entropy alloys, Phys. Rev. X 5 (1) (2015) 1–6.
[9] S.J. Zinkle, L.L. Snead, Designing radiation resistance in materials for fusion energy, Annu. Rev. Mater. Res. 44 (1) (2014) 241–267.
[10] A. Ayyagari, R. Salloom, S. Muskeri, S. Mukherjee, Low activation high entropy alloys for next generation nuclear applications, Materialia 4 (September) (2018) 99–103.
[11] M.R. Gilbert, M. Fleming, J.-C. Sublet, Automated inventory and material science scoping calculations under fission and fusion conditions, in: In International Conference On Mathematics & Computational Methods Applied To Nuclear Science & Engineering, 2017.
[12] M.R. Gilbert, M. Fleming, J.C. Sublet, Automated inventory and material science scoping calculations under fission and fusion conditions, Nucl. Eng. Technol. 49 (6) (2017) 1346–1353.
[13] P.J. Barron, A.W. Carruthers, J.W. Fellowes, N.G. Jones, H. Dawson, E.J. Pickering, Towards V-based high-entropy alloys for nuclear fusion applications, Scripta Mater. 176 (2020) 12–16.
[14] M.R. Gilbert, et al., Waste implications from minor impurities in European DEMO materials, Nucl. Fusion 59 (7) (2019).
[15] M.W. Ullah, D.S. Aidhy, Y. Zhang, W.J. Weber, Acta Materialia Damage accumulation in ion-irradiated Ni-based concentrated solid-solution alloys, Acta Mater. 109 (2016) 17–22.
[16] Y. Zhang, et al., Influence of chemical disorder on energy dissipation and defect evolution in concentrated solid solution alloys, Nat. Commun. 6 (1) (2015), 8736.
[17] D.S. Aidhy, et al., Acta Materialia Point defect evolution in Ni , NiFe and NiCr alloys from atomistic simulations and irradiation experiments, Acta Mater. 99 (2015) 69–76.
[18] G.D. Samolyuk, R.E. Stoller, L.K. Beland, Differences in the accumulation of ion-beam damage in Ni and NiFe explained by atomistic simulations, J. Alloys Compd. 662 (2016) 415–420.
[19] K. Jin, et al., Acta Materialia Effects of Fe concentration on the ion-irradiation induced defect evolution and hardening in Ni-Fe solid solution alloys, Acta Mater. 121 (2016) 365–373.
[20] T. Yang, et al., Acta Materialia Effect of alloying elements on defect evolution in Ni-20X binary alloys, Acta Mater. 151 (2018) 159–168.
[21] D.B. Miracle, O.N. Senkov, A critical review of high entropy alloys and related concepts, Acta Mater. 122 (2017) 448–511.
[22] K.Y. Tsai, M.H. Tsai, J.W. Yeh, Sluggish diffusion in Co-Cr-Fe-Mn-Ni high-entropy alloys, Acta Mater. 61 (13) (2013) 4887–4897.
[23] J. Dąbrowa, et al., Demystifying the sluggish diffusion effect in high entropy alloys, J. Alloys Compd. 783 (2019) 193–207.
[24] N. Saunders, A.P. Miodownik, CALPHAD: Calculation of Phase Diagrams A Comprehensive Guide, vol. 1, 1998.
[25] K.A. Christo, et al., Intermetallics on the in fl uence of Mn on the phase stability of the CrMn x FeCoNi high entropy alloys 92 (2018) 84–92. August 2017.
[26] J. Joubert, G. Bracq, M. Laurent-brocq, L. Perri, I. Guillot, Acta Materialia the fcc solid solution stability in the Co-Cr-Fe-Mn-Ni multi-component system re 128, R e my Pir e, 2017.
[27] M.E. Bloom, K.A. Christo, N.G. Jones, Intermetallics E ff ect of Co on the phase stability of CrMnFeCo x Ni high entropy alloys following long-duration exposures at intermediate temperatures 114, July, 2019.
[28] K.A. Christo, T.P. Mcauliffe, P.M. Mignanelli, H.J. Stone, N.G. Jones, On the prediction and the formation of the sigma phase in CrMnCoFeNi x high entropy alloys 770 (2019) 285–293.
[29] P.J. Spencer, J.N. Pratt, A study of the vapour pressure of manganese using a new high-temperature torsion - effusion apparatus, Br. J. Appl. Phys. 18 (10) (1967) 1473–1478.
[30] F.A. Stevie, et al., Application of focused ion beam lift-out specimen preparation to TEM, SEM, STEM, AES and SIMS analysis, Surf. Interface Anal. 31 (5) (2001) 345–351.
[31] H.W. Kerr, W. Kurz, Solidification of Peritectic Alloys Solidification of Peritectic Alloys, June, 2014.
[32] D.A. Porter, K.E. Easterling, M.Y. Shefir, Phase Transformations in Metals and Alloys 3 (1) (2009).
[33] N. Yurchenko, E. Panina, M. Tikhonovsky, G. Salishchev, S. Zherebtsov, N. Stepanov, Structure and mechanical properties of an in situ refractory Al 20 Cr 10 Nb 15 Ti 20 V 25 Zr 10 high entropy alloy composite, Mater. Lett. 264 (2020) 127372.
[34] R.K. Song, L.J. Wei, C.X. Yang, S.J. Wu, Phase formation and strengthening mechanisms in a dual-phase nanocrystalline CrMnFeVTi high-entropy alloy with ultrahigh hardness, J. Alloys Compd. 744 (2018) 552–560.
[35] "PDF-4+ 2016." International Centre for Diffraction Data.
[36] T.B. Massaiski, J.L. Murray, L.H. Bennet, H. Baker, Binary Alloy Phase Diagrams, s vols. 1 and 2, American Society for Metals, Ohio, 1986.
[37] C.T. Liu, J.H. Zhu, M.P. Brady, C.G. McKamey, L.M. Pike, Physical metallurgy and mechanical properties of transition-metal Laves phase alloys, Intermetallics 8 (9–11) (2000) 1119–1129.
[38] J.H. Zhu, L.M. Pike, C.T. Liu, P.K. Liaw, Point defects in binary Laves phase alloys, Acta Mater. 47 (7) (1999) 2003–2018.
[39] A.J. Knowles, et al., Data on a Laves phase intermetallic matrix composite in situ toughened by ductile precipitates, Data Br. 14 (2017) 489–493.